scientific reports

Check for updates

OPEN

Obstacle inversion based on the self-healing property of structured light

Shuailing Wang[1,3], Zhe Zhao[1,3], Mingjian Cheng[2], Jingping Xu[1]✉ & Yaping Yang[1]✉

The self-healing property of structured light allows it to partially recover its original intensity distribution during propagation after a portion of its intensity has been obscured by an obstacle. In this study, we present a thorough investigation of the self-healing property of perfect vortex beam (PVB) within structured light. Firstly, we investigated the impact of obstacles of varying sizes and shapes on PVB at different stages of propagation, leading to a key conclusion the self-healing process of PVB can be divided into two parts: the self-healing of the obstructed region and the damage in the unstructured region. Secondly, we propose a novel structural metric as a precise and quantitative description of the self-healing property of structured light, equipped with adjustable parameters to cater to different self-healing demands. We also undertake an exploration of the self-healing mechanisms of structured light, utilizing the theory of wave-particle duality. Thirdly, drawing from our research findings, we propose a novel optical application model for obstacle inversion based on the self-healing property of structured light. This model accurately inverts the size and position of obstacles. Furthermore, we integrate convolutional neural networks into our obstacle inversion model, enabling successful inversion of obstacle size and position, even in scenarios with significant variations in the intensity information of structured light caused by oceanic turbulence. Our research has not only enhanced the comprehension of the self-healing mechanisms in structured light, but also established new avenues for its implementation in optical imaging, obstacle detection, and other fields.

The self-healing property, also referred to as the self-reconstruction property, is an intriguing phenomenon of structured light that enables it to restore and reconstruct the intensity distribution of an obstructed region during its subsequent propagation beyond an obstacle. The earliest discovery of this property can be traced back to MacDonald et al.'s experimentation with Bessel beams, where they observed the intriguing phenomenon that the central spot of the Bessel beams could self-healing even after being obstructed by an obstacle[1]. In 1998, Bouchal et al. further probed into the self-healing property exhibited by Bessel beams, demonstrating that Bessel beams can reconstruct their initial amplitude distribution in free space propagation after encountering an obstacle[2]. As the research into structured light has progressed, inspired by the self-healing property exhibited by Bessel beams[3], researchers have explored both theoretically and experimentally whether Airy beams possess a similar self-healing property. It has been demonstrated that Airy beams do exhibit the self-healing property[4]. Following this, researchers have extensively studied the Airy beam family, and the self-healing property has been observed in various types of Airy beams, including but not limited to cosh-Airy beams[5], circular Airy beams[6], Airy arrays beams[7], and circular Airy derivative beams[8].

Along with discovering the self-healing property of structured light, efforts have been devoted to providing theoretical explanations and developing methods for quantifying this unique property. Theoretical explanations for the self-healing property of structured light primarily fall into three categories: Babinet's principle[2], caustic theory[9,10], and wave optics theory[11]. Drawing upon experimental results and theoretical explanations for the self-healing property, it is widely recognized that the effectiveness of the self-healing property primarily depends on the specific engineered beam structure[12,13]. As a result, in many cases, the self-healing property of structured light is highly sensitive to the size and shape of obstacles encountered. Researching the impact of obstacles of differing sizes and shapes on the self-healing property of structured light is an essential area of inquiry. Researchers have utilized cosine similarity as a quantification measure for the degree of self-healing in structured light[14,15]. This measure provides a specific percentage to illuminate the degree of self-healing, offering a tool for comparing the self-healing property among different types of structured light in a quantifiable manner. However, much like how individuals assess image similarity differently based on their visual system—

[1]School of Physics Science and Engineering, Tongji University, Shanghai 200092, China. [2]School of Physics, Xidian University, Xi'an 710071, China. [3]Shuailing Wang and Zhe Zhao contributed equally to this work. ✉email: xx_jj_pp@tongji.edu.cn; yang_yaping@tongji.edu.cn

emphasizing luminance, structure, or contrast to varying degrees—the evaluation of structured light self-healing should not be confined to a single metric. Rather, it necessitates a comprehensive evaluation that considers the interplay of multiple factors, including luminance, contrast, and structure of structured light. Given this, a scientifically rigorous similarity metric to quantify the degree of self-healing becomes particularly important.

Being one of the most significant properties of structured light, the self-healing property has been employed in optical applications. The self-healing property has been instrumental in the ability of optical tweezers to trap particles in multiple, spatially separated sample cells with a single beam[16]. In quantum optics, the self-healing property of structured light can effectively overcome the losses resulting from obstacles in quantum entanglement, thus once again revealing the entanglement after propagation beyond the obstruction[17–20]. However, the practical optical applications of the self-healing property are relatively less extensive compared with other properties of structured light, such as orbital angular momentum (OAM), anti-diffraction property, perfect property, and so on[21]. The perfect vortex beam (PVB), as an advanced form of structured light, has garnered considerable attention from researchers since its introduction[22,23]. This interest stems primarily from the inherent limitations of conventional structured light, such as Bessel beams, whose beam radius increases significantly with rising OAM. This expansion leads to a progressive degradation in the optical performance of structured light as OAM increases, severely constraining the practical applications of high-order structured light[24,25]. Additionally, the larger beam size imposes more stringent demands on experimental systems and optical instrumentation. The advent of PVB, whose beam radius remains nearly invariant with respect to OAM, effectively addresses these challenges, thereby significantly enhancing the viability and performance of high-order structured light in diverse optical applications. As a result, PVB are widely regarded as the future of structured light[26–30]. Henceforth, in the present work, the PVB serves as the vehicle through which we investigate the self-healing property of structured light.

In this research, our work is primarily structured into four principal sections. Firstly, we investigate the self-healing property of the PVB through a comprehensive analysis of various obstacles, featuring different sizes and shapes - such as rectangles, fans, circles, and dots - and their impact on the beam at different stages of propagation. Furthermore, we present five corresponding conclusions that summarize the key findings of this comprehensive study. In the second section, we present a structural similarity metric that is used to evaluate the degree of self-healing of structured light, consequently enabling a more accurate quantification of structured light's self-healing property. Furthermore, based on our research findings, we discussed the self-healing mechanism of structured light by making use of wave-particle duality. In the Third section, drawing upon the preceding research findings, we propose an optical application model for obstacle inversion, utilizing the self-healing property of structured light. With the aid of our proposed model, the size and position of obstacles can be accurately inverted. Furthermore, we have integrated the convolutional neural networks (CNN) into the obstacle inversion model, enabling the successful inversion of obstacle size and location even under oceanic turbulence conditions, where the intensity information of structured light is severely distorted.

Results
Influence of obstacles with different shapes on the self-healing property
As shown in Fig. 1, we placed an obstacle mask along the propagation path of a PVB. The shape of the obstacles was controlled by adjusting the obstacle mask, and the self-healing property of the PVB were observed on the receiving plane. We examined the self-healing property of PVB under various obstacle conditions by generating four different types of obstacles, including rectangle, fan, circle, and dot. Our investigation revealed significant differences in the self-healing property of the PVB under various obstacle conditions. Specifically, PVB exhibited improved restoration effects under the influence of obstacles in the form of circles, while rectangles, fans and dots resulted in relatively poorer performance for PVB. The effect of the circle obstacle on PVB shows different restoration effects in intensity and shape. While the restoration effect appeared to be unsatisfactory in terms of intensity, the PVB maintained a well-defined circular ring structure which outperformed the rectangle, fan and dot obstacles. Thus, our findings suggest that a comprehensive assessment of the self-healing property of the PVB should involve the quantification of restoration effects both in terms of intensity and shape, rather than solely assessing either one of these aspects. It is important to note that the self-healing property of PVB is not a simple recovery of the obscured region, but rather depend on the distinct energy flow of PVB under different obstacle conditions, consequently leading to different restoration effects.

Subsequently, we conducted a comprehensive investigation on the impact of obstacles with different shapes on the self-healing property of the PVB. As it is well-known, the propagation of the PVB occurs in two distinct stages, known as the anti-diffraction stage and the self-focusing stage. Therefore, we conducted a study on the self-healing property of PVB at different distances following its passage through rectangular obstacles of varying widths, as depicted in Fig. 2. The PVB exhibits a certain degree of self-healing property in both the anti-diffraction and self-focusing stages, resulting in partial recovery of the obstructed region in terms of shape and intensity. Particularly, the central region in the self-focusing stage has almost achieved a similar intensity to the unobstructed PVB, indicating an excellent restoration effect. However, it should be noted that, although the intensity obstructed region is continuously being restored, the unobstructed region is subjected to damage due to the influence of the obstacles. During the transition from the anti-diffraction stage to the self-focusing stage, we observed severe damage to the unobstructed region, displaying a significant intensity distribution in a fish-tail shape. Furthermore, the self-healing property of structured light is subject to certain limitations. We observed a notable decline in the ability to restore the shape and intensity of the obstructed region as the obstacles increased in size. Moreover, we investigated the self-healing property of the PVB by reducing the length of the rectangular obstacles to enable partial transmission of PVB's ring intensity. Despite observing a certain improvement in the self-healing property, the unobstructed region still experienced damage represented by the fish-tail pattern. It is important to note that we observed the obstruction of the obstacles could lead to a redistribution of energy in
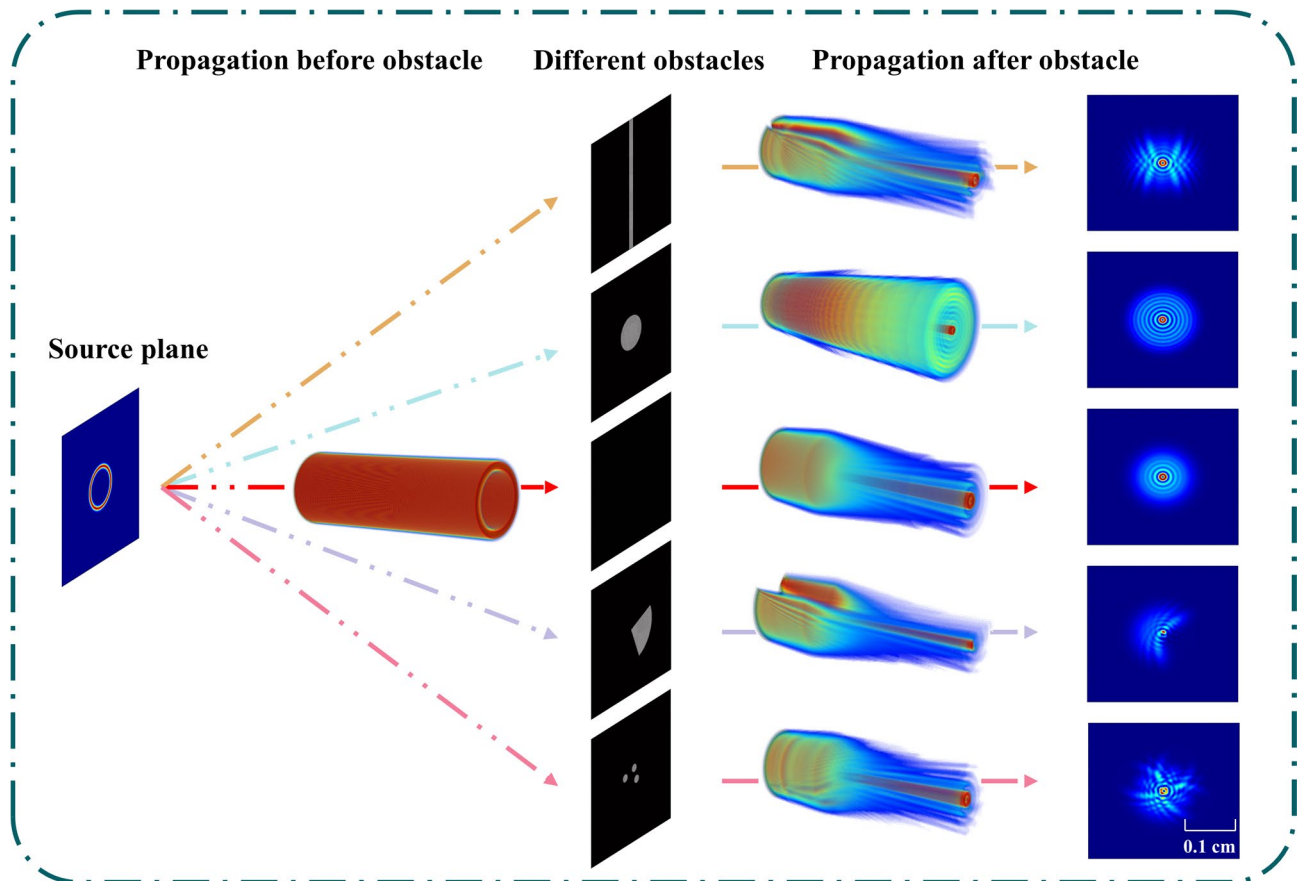
Fig. 1. The restoration effect of the PVB under the influence of various obstacles. The types of obstacles include: rectangles, fans, circles, and dots.

the unobstructed region of the PVB, resulting in their aggregation around the obstacles. This finding indicates the potential utilization of the self-healing property of PVB in optical trapping since the addition of obstacles on the PVB could actively alter the intensity distribution, allowing accurate manipulation of particles. As shown in Fig. 3, variations in the position of rectangular obstacles result in a tendency for the recovered intensity distribution of the PVB to shift toward the unobstructed region. Moreover, as the number of rectangular obstacles increases, the quality of PVB recovery gradually degrades. This phenomenon primarily arises from the increased obstruction of the beam's intensity distribution, which reduces the available information required for recovery. In addition, we further investigated the influence of obstacle placement at different positions on the self-healing behavior of the PVB. The results indicate that, regardless of whether the obstacles are located during the anti-diffracting stage or the self-focusing stage, the intensity distribution of the PVB exhibits a certain degree of recovery with increasing propagation distance.

In Fig. 4, we investigated the influence of circle obstacles on the self-healing property of PVB. At $z = 4$ cm, the circle obstacles exhibited a superior capacity to restore the shape and intensity of the obstructed region of PVB in comparison to rectangular obstacles. However, an interesting observation was that due to the obstruction of the obstacles, the central ring, which was supposed to appear during the self-focusing stage, appeared earlier at the anti-diffraction stage. Similar to the rectangular obstacles, the unobstructed region of PVB also suffered severe damage consequent to the influence of circle obstacles. Moreover, we devised an anti-circle obstacle that acted as a circle aperture for PVB propagation. A fascinating phenomenon was observed, whereby PVB retained its anti-diffraction and self-focusing stages during propagation under the influence of obstacles of other shapes. However, under the influence of the anti-circle obstacle, the propagation of PVB no longer exhibited a self-focusing property but transformed completely into a Bessel-like Gaussian beam as it propagated. Furthermore, upon reducing the size of the circle aperture, PVB transformed further into a Bessel-like beam. Taking into account both Figs. 2 and 4, three conclusions can be reached: 1) PVB's self-healing property require the preservation of as much circular intensity information as possible, as seen in the restoration of PVB under the influence of circle obstacle being better compared to rectangular obstacle, because the circular structure of PVB is preserved to a certain extent by the circle obstacle. 2) the self-healing property of PVB exhibit a limit; after reaching the self-focusing stage, the restoration effect of PVB tends to stabilize, and there is almost no significant change in its shape even after further propagation. 3) the self-healing property of PVB exhibited a trend of initial reduction followed by an increase under the influence of rectangular obstacle. This is markedly different from
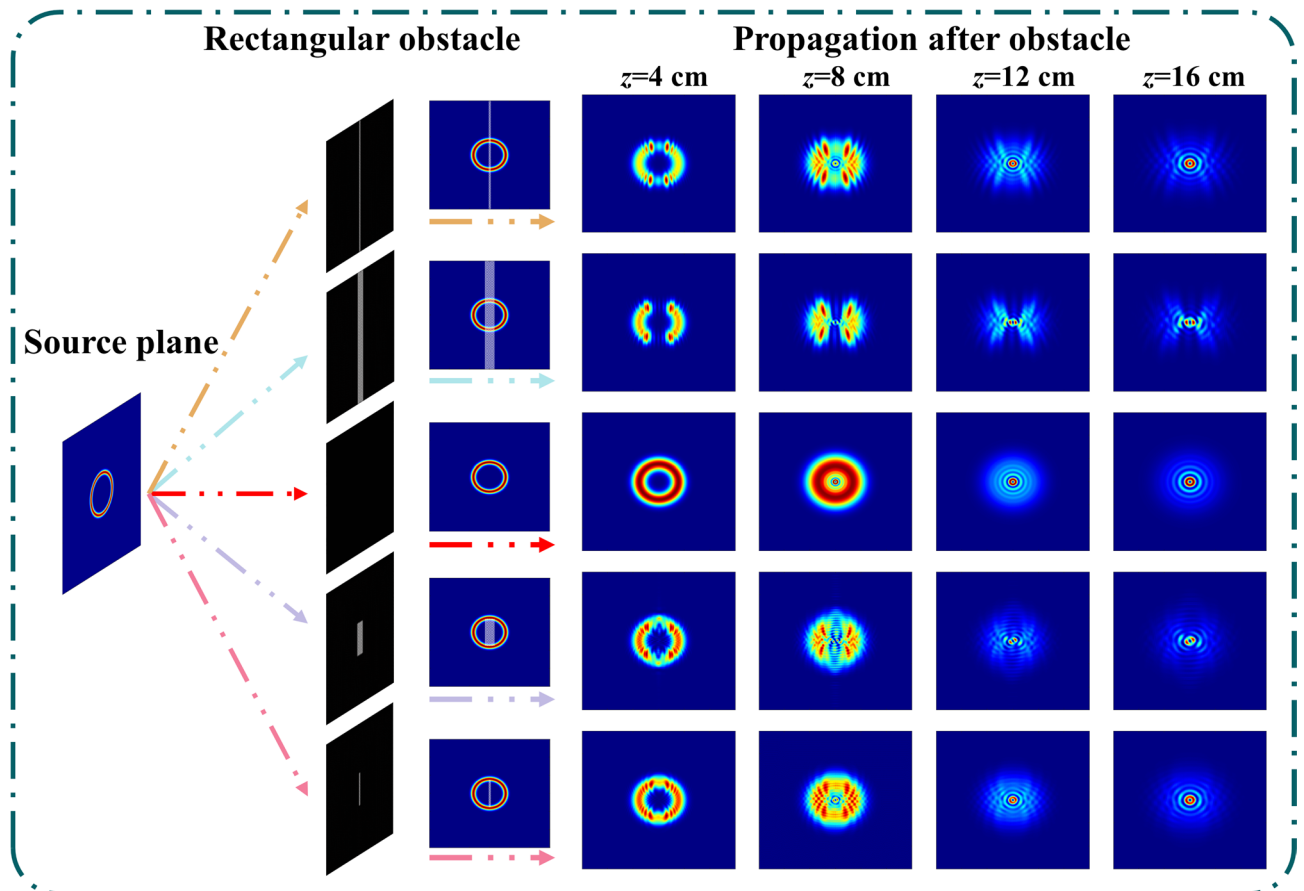
Fig. 2. The intensity evolution of PVB after passing through rectangular obstacles of varying sizes. Here, z represents the receiving plane at different positions.

other structured light' self-healing property, which typically display a direct upward trend. PVB's self-focusing property seems to have weakened its self-healing property.

The impact of fan-shaped and dot-shaped obstacles on the self-healing property of PVB was also explored in Fig. 5. As can be seen from Fig. 5(a), the outer ring energy of the PVB that is not obstructed by the fan-shaped obstacle, behaves similarly to that under the influence of rectangular obstacle, with the energy converging at the two ends of the obstacle. When the size of the obstacle is small, the central ring of PVB in the self-focusing stage can be restored. However, as the size of the fan-shaped obstacle further increases, the shape of the central ring is no longer maintained as a ring. It is noteworthy that the energy of the central ring in PVB under the influence of fan-shaped obstacles is focused only on one side, in contrast to the primarily localized energy at both ends of the obstacle observed under the influence of rectangular obstacles. Observations indicate that as the radius of the fan-shaped obstacle decreases to a point where PVB's intensity distribution can retain some ring-shaped information. There is a slight improvement in the overall shape of PVB than when the radius of fan-shaped obstacle is too large, but the restoration effect is not as pronounced as in the presence of circular obstacles. The intensity distribution of PVB in self-focusing stage exhibits a shell-shaped pattern under the influence of fan-shaped obstacles. The dot-shaped obstacle section in Fig. 5(b) revealed that during the anti-diffraction stage, the overall intensity of the unobstructed region is lower when the dot-shaped obstacle is positioned within the circular region compared to the scenario where the dot-shaped obstructs the ring. This difference in intensity may be attributed to the reason that when the dot is positioned within the circular region, more energy is directed towards restoring the obstructed region, and the energy to be focused at both sides of the obstacle. In the self-focusing stage, due to PVB preserving more energy under the influence of smaller obstacles, the restoration effect of the dot-shaped obstacle within the circular region is significantly better than that of the dot-shaped obstacle obstructing the ring. When the number of dot-shaped obstacles increases, it further undermines the restoration effect of PVB. Therefore, based on the results in Figs. 2 and 5, we can draw the remaining two conclusions: 4) when obstacles obstruct the ring structure of PVB, energy in the unobstructed regions is focused towards both ends of the obstacle; 5) the self-healing process of PVB should be divided into two parts - healing in the obstructed region and damage in the unstructured region. According to our conclusions, the characteristic of the energy in the unobstructed region of PVB being focused toward both ends of an obstacle could have potential applications in optical trapping. By deliberately introducing obstacles within PVB, it may be possible to achieve control of particles. It is important to note that this study on the self-healing property of PVB primarily focuses on theoretical exploration. In the development of the theoretical model, idealized assumptions and approximations
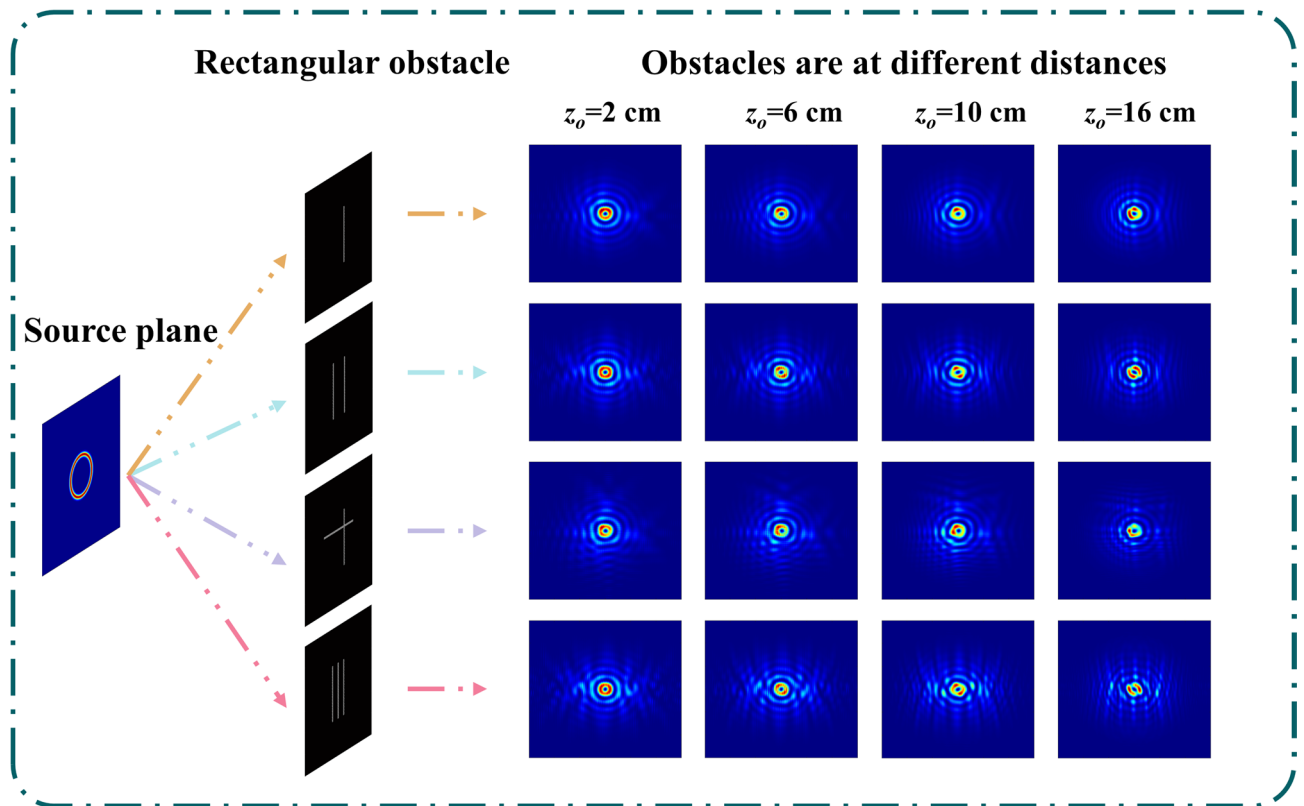
Fig. 3. The impact of varying numbers of rectangular obstacles placed at different positions and propagation distances on the intensity distribution of the PVB. Here, z_o represents the obstacles are in different propagation distances.

were employed, which, while facilitating the optimization of the analysis process, may introduce deviations from the actual propagation behavior of the PVB. Furthermore, due to the limitations of mathematical model accuracy and computational resources, systematic errors may accumulate as the model's complexity increases. Nevertheless, our research provides a solid theoretical framework for understanding the self-healing property of PVB and offers valuable insights to guide subsequent experimental investigations.

Structural similarity of structured light

Through the study of the influence of different obstacles on PVB's self-healing property, we have found that in an ideal free space, although PVB's shape and intensity change with the transmission distance, the overall intensity change of PVB under the influence of obstacles is solely dependent on the size of the obstacle. As shown in Fig. 6(a), the intensity ratio of PVB remains constant as the propagation distance increases, providing a reliable basis for the application development of PVB's self-healing property. Here, the term intensity ratio refers to the ratio of the self-healing intensity of PVB affected by obstacles to that of the original intensity of PVB unobstructed by obstacles. Through the analysis of the self-healing evolution of PVB under diverse types of obstacles, we have observed that the restoration effect induced by different obstacles on the intensity and shape of PVB vary significantly. Therefore, we attempt to propose a self-healing metric to quantify the performance of PVB's self-healing property. This metric should not only compare the intensity of PVB that is and is not affected by obstacles but also include the similarity in shape between the two states of PVB. Here, we adopt the concept of structural similarity (SSIM) commonly used in image quality assessment to design a self-healing index for PVB. The SSIM typically divides the task of measuring similarity into three distinct components: luminance, contrast, and structure[31]. Therefore, in structured light, we follow this design philosophy. But the difference is that here, we will reconstruct and design the SSIM according to the features of structured light during its self-healing evolution.

The design of the SSIM for structured light begins with the consideration of luminance, our first step is to obtain the original intensity of the unobstructed PVB and the self-healing intensity of the PVB that has been affected by obstacles. These two field intensities need to be aligned with each other while maintaining the same size. Next, we assume that the intensity is discrete and extract the corresponding mean intensities μ_x and μ_y from this intensity. By doing so, we derive a luminance comparison function that has a correlation with μ_x and μ_y,

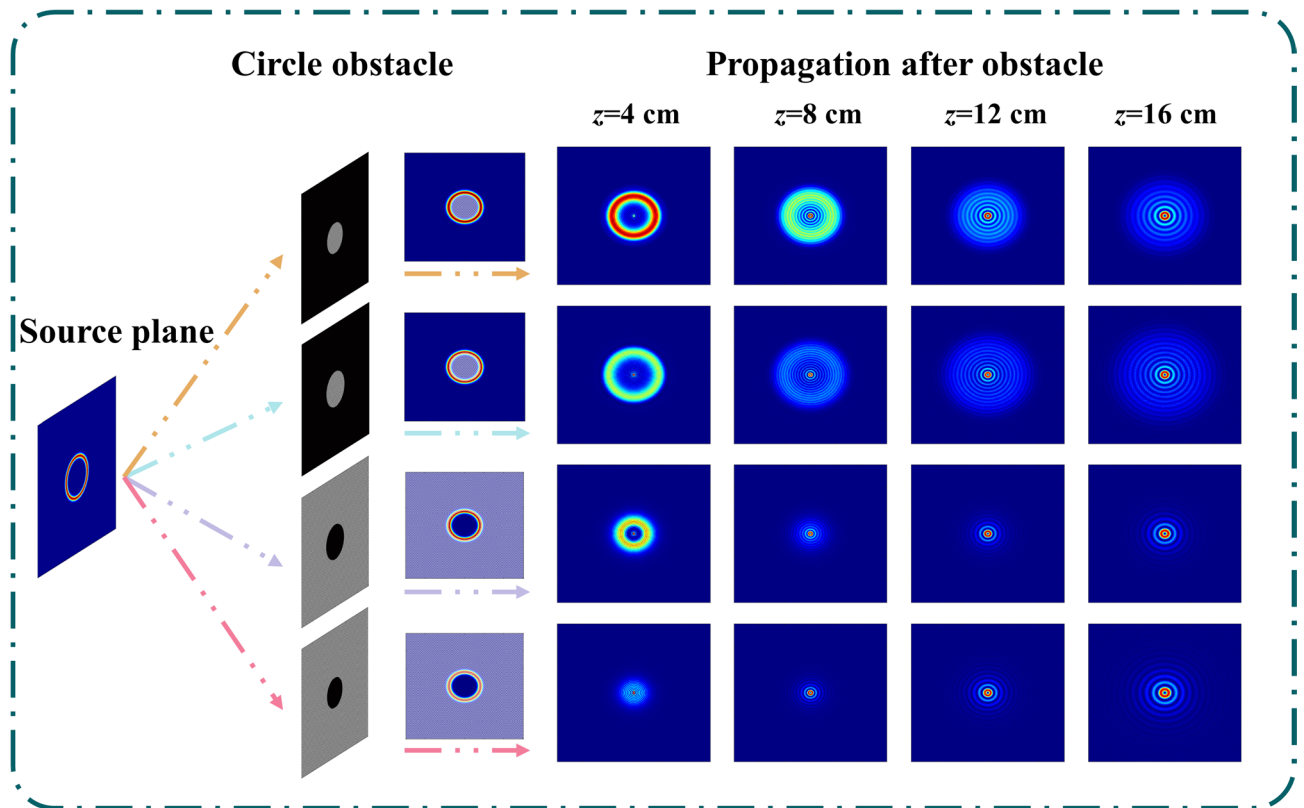$$l(x,y) = \frac{\mu_x + c_1}{\mu_y + c_1}. \tag{1}$$

Fig. 4. Intensity evolution of PVB under the influence of circle obstacles with different radius. The first two rows consist of circle obstacles, whereas the last two rows contain anti-circle obstacles.
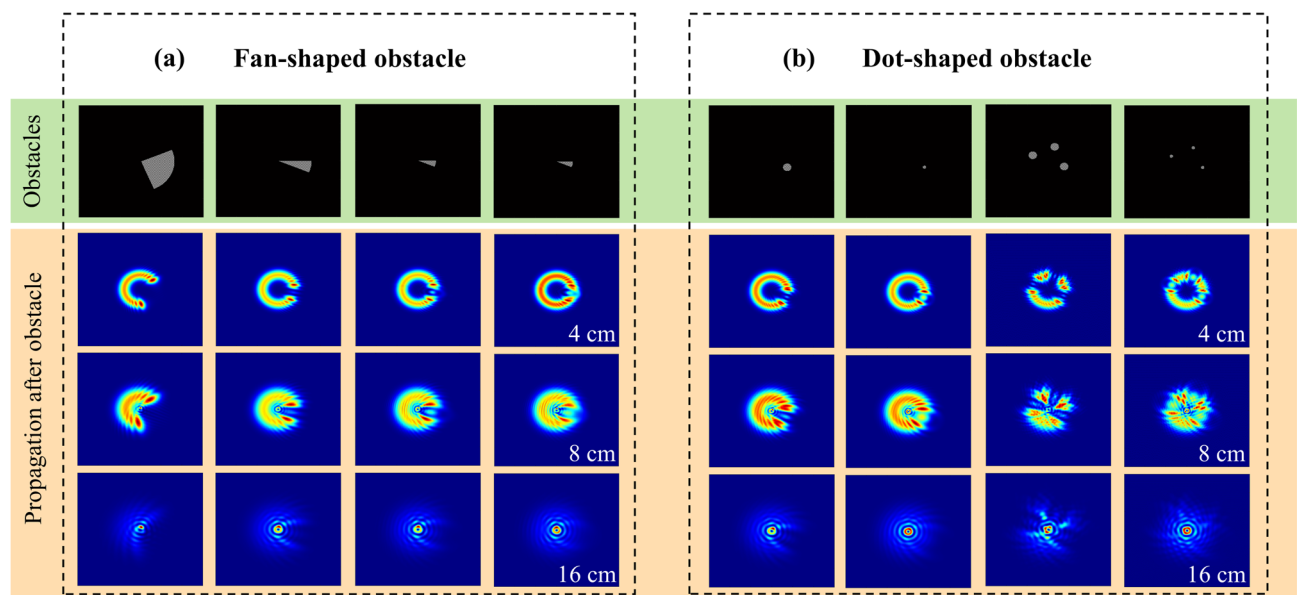

Fig. 5. The intensity distribution of PVB after propagating through (**a**) fan-shaped obstacle and (**b**) dot-shaped obstacle of different sizes.

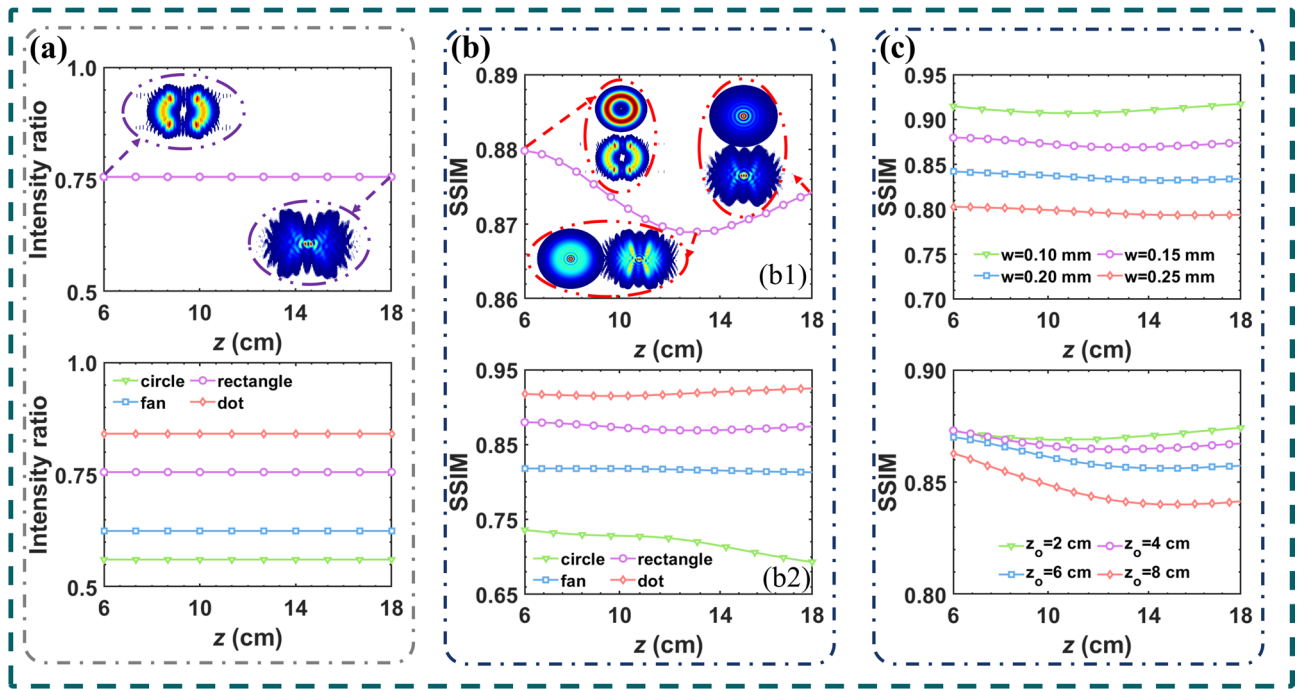**Fig. 6.** (**a**) The intensity ratio of PVB varies with the propagation distance under the influence of different obstacles. (**b**) The evolution of SSIM as a function of propagation distance for PVB is influenced by various obstacles. (**c**) The evolution of the SSIM of the PVB with respect to propagation distance under varying obstacle widths and obstacle positions along the propagation path.

Secondly, the standard deviation reflects the distribution of the field intensity within its dynamic range. A broader distribution of field intensity is indicated by a larger standard deviation. To this end, we construct a contrast comparison function using the standard deviations σ_x and σ_y:

$$c\left(x, y\right) = \frac{\sigma_x \sigma_y + c_2}{\sigma_y^2 + c_2}. \tag{2}$$

where c_1 and c_2 are constants. Thirdly, Euclidean distance is the most commonly used distance measurement in image recognition, and it measures the absolute distance between points in a multi-dimensional space. Here, we utilize the Euclidean distance to estimate the structure of X and Y, where X denotes the self-healing intensity of the structured light, Y represents the original intensity. A larger Euclidean distance between the two indicates a more significant structural difference between them. X and Y first need to be converted into vectors $v_x = vec(X), v_y = vec(Y)$ for further computation. Here, vec refers to the process of transforming the intensity information into a vector form, and the structural comparison function will be constructed as follows:

$$s\left(x, y\right) = 1 - \frac{\|v_y - v_x\|^2 + c_3}{\|v_y\|^2 + c_3}. \tag{3}$$

In this context, c_i is a constant introduced to avoid potential issues when the denominator approaches zero. Specifically, we choose:

$$c_i = \frac{K_i}{L}, \tag{4}$$

where $K_1 = 0.01 \times 10^{-6}$, $K_2 = 0.03 \times 10^{-6}$, $K_3 = 0.015 \times 10^{-6}$, L indicates the total number of pixels in either image X or Y.

Finally, the luminance comparison function, contrast comparison function, and structure comparison function are combined together, and name the resulting similarity measure the SSIM of structured light between intensity X or Y.

$$SSIM\left(x, y\right) = \frac{l\left(x, y\right) \alpha + c\left(x, y\right) \beta + s\left(x, y\right) \gamma}{\alpha + \beta + \gamma}. \tag{5}$$

The parameters α, β, γ are utilized to regulate and balance the relative importance of each comparison function, which can be adjusted reasonably according to the desired degree of self-healing in terms of luminance, contrast,

and structure. Our reconstructed structured light's SSIM satisfies boundedness $0 \leqslant SSIM(x,y) \leqslant 1$, with its maximum value attained if and only if $X = Y$, and the minimum value attained if and only if the obstacle sufficiently covers the entire structured light. The SSIM of structured light can effectively serve as an evaluation metric for the self-healing performance of all structured light with self-healing property.

In Fig. 6(b1), we quantified the self-healing property of a rectangular obstacle using SSIM. The evolution of the SSIM line segments indicates a good fit with the actual changes in self-healing intensity of structured light. The SSIM of PVB exhibits a decreasing-then-increasing trend in the presence of a rectangular obstacle, which is attributed to a superposition of changes in intensity caused by the obstacle and stage conversion when the intensity structure of PVB transitions from the anti-diffraction stage to the self-focusing stage. The resulting coincidence of changes in intensity leads to the worst SSIM. As shown in Fig. 6(b2), the evolution of SSIM for different obstacles varies significantly. This highlights the importance of studying the impact of different obstacles on the self-healing property of PVB, given the dissimilarities in restoration effect of PVB among various obstacles, and even between various sizes of the same type of obstacle. Therefore, specific analyses must be conducted with consideration of the particular situations. As shown in Fig. 6(c), the SSIM of the PVB exhibits a continuous decline with increasing obstacle width. This result is consistent with our theoretical expectations, as a wider obstacle blocks a larger portion of the beam's intensity, thereby significantly reducing the effective intensity distribution available for the self-healing process, and ultimately diminishing the beam's self-healing performance. Furthermore, we further investigated the influence of obstacle placement along the propagation axis on the self-healing property of the PVB. The results indicate that as the obstacle is positioned further away from the source plane, the SSIM of the PVB gradually decreases, suggesting a degradation in its self-healing performance. This phenomenon can be primarily attributed to two factors: first, the natural transverse expansion of the PVB during propagation increases the proportion of the intensity profile obstructed by a fixed-size obstacle placed at longer distances; second, the increased distance of the obstacle shortens the available propagation length behind it, thereby limiting the intensity redistribution process guided by edge diffraction and ultimately weakening the intensity reconstruction of the beam. We have established a comprehensive model that investigates the self-healing intensity evolution of structured light under various shaped obstacles, along with the corresponding evaluation metric, SSIM of structured light. These studies provide a solid foundation and more in-depth research can subsequently be conducted in this field.

As previously mentioned, we have concluded from the intensity evolution of PVB that PVB's self-healing process can be divided into two distinct components: one pertains to the self-healing of the obstructed region, while the other pertains to the damage in the unobstructed region. We performed a quantification of this conclusion using SSIM of structured light. In Fig. 7(a), we present the self-healing process of the PVB in two distinct regions: the obstructed region and the unobstructed region. As shown in Fig. 7(a), with increasing propagation distance, the intensity and shape of the obstructed region gradually recover, whereas the intensity distribution of the unobstructed region experiences some degree of distortion due to the influence of the obstacle. Figure 7(b) further illustrates that as the propagation distance increases, the SSIM of the obstructed region steadily rises, while the SSIM of the unobstructed region gradually decreases. This observation serves as a full validation of our previous conclusion. The combined effect of intensity variations in both the obstructed and unobstructed regions contributes to the overall evolution of SSIM. Furthermore, in Fig. 7(c), we compare the original SSIM (SSIM for image quality assessment), cosine similarity, and our proposed SSIM. When the PVB first encounters the obstacle, the similarity should measure the degree of resemblance between the PVB affected by the obstacle
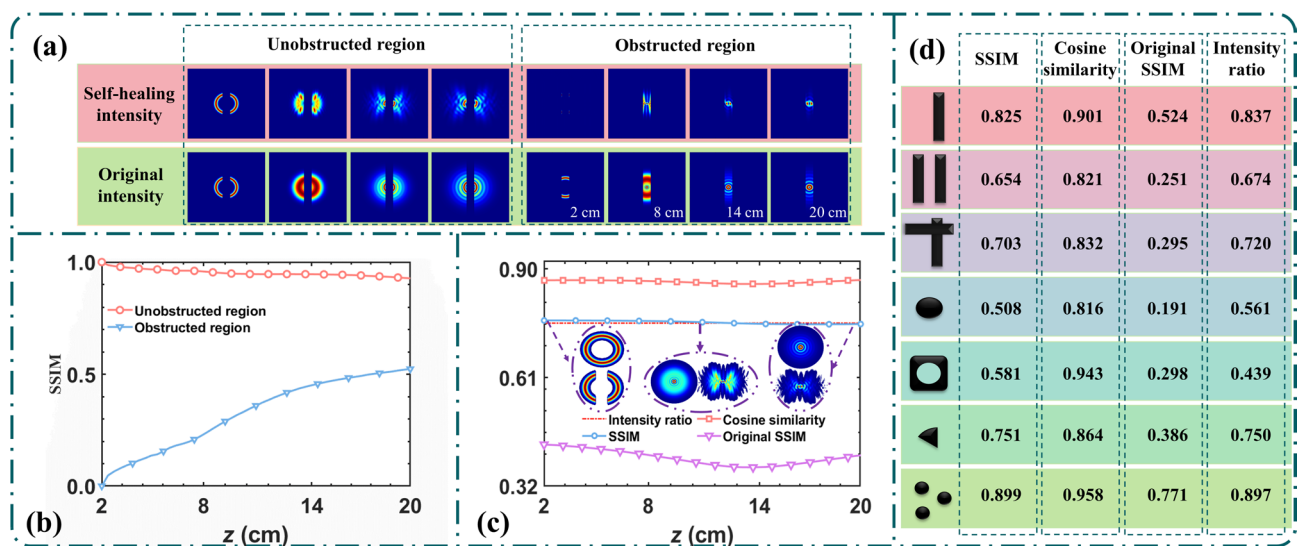

Fig. 7. (**a**) The self-healing intensity distribution and original intensity distribution in the unobstructed region and obstructed region. (**b**) The evolution of SSIM with propagation distance in unobstructed region and obstructed region. (**c**) The evolution of SSIM for image quality, cosine similarity and SSIM with propagation distance. (**d**) A comparison of SSIM and other similarity metrics under different types of obstacles.

and the unaffected PVB. Theoretically, the similarity value at this point should be approximately equal to the intensity ratio. The red dashed line in the figure represents this intensity ratio. As shown in Fig. 7(c), at the initial encounter with the obstacle, the cosine similarity is significantly higher than the intensity ratio, whereas the conventional SSIM used for image quality assessment is notably lower. In contrast, our redesigned SSIM, specifically tailored to the characteristics of structured light, closely aligns with the intensity ratio. Moreover, throughout the subsequent propagation process, the evolution trend of our proposed SSIM more accurately reflects the actual variations of the PVB compared to both cosine similarity and original SSIM, demonstrating its enhanced capability to characterize the self-healing dynamics of structured light. Furthermore, as illustrated in Fig. 7(d), we present a comparative analysis of various metrics under different types of obstacles, including the proposed SSIM, cosine similarity, original SSIM, and intensity ratio. The results demonstrate that the proposed SSIM consistently exhibits a more coherent response to the self-healing property of PVB across all obstacle types, thereby further validating its effectiveness in characterizing the self-healing dynamics of structured light.

It is noteworthy that during the self-healing process, the constant intensity ratio and the continuously evolving SSIM of PVB reflect the wave-particle duality of structured light. On one hand, PVB exhibit the wave nature of light. When the beam is partially obstructed, edge diffraction occurs, allowing residual intensity to bend around the edges of the obstacle—much like water waves flowing past a barrier. This diffraction-driven mechanism enables the energy to spread into the geometric shadow region, resulting in the partial reconstruction of both the beam's intensity and structural profile in the obstructed region. On the other hand, PVB also demonstrate the particle nature of light. Their propagation adheres to the principle of energy conservation: when part of the beam is blocked by an obstacle, the number of photons in the remaining beam remains constant during the self-healing process. Furthermore, the total number of remaining photons in the beam decreases as the level of obstruction increases. Just as lost particles do not regenerate over distance, the photons blocked by the obstacle do not reappear as a result of self-healing. This interplay between edge diffraction and energy conservation constitutes a fundamental aspect of the self-healing dynamics in PVB. Hence, we draw the sixth conclusion regarding the self-healing property of structured light: 6) The self-healing of structured light is not the regeneration of the obstructed region. Instead, the self-healing process is primarily associated with the redistribution of energy in the unobstructed region of the structured light. This finding is of paramount importance in the comprehensive understanding of the self-healing mechanisms of structured light.

Obstacle inversion based on the self-healing property of structured light

In contrast to the extensive optical applications developed based on the OAM, anti-diffraction property, and perfect property of structured light, few applications have been explored based on the self-healing property of structured light. Presently, research on the self-healing property of structured light is primarily focused on theoretical investigation and experimental explorations of the self-healing phenomenon. Herein, we present an optical application of obstacle inversion based on the self-healing property of structured light, utilizing the conclusions derived from our study on the self-healing property of structured light, as well as the SSIM that we have devised.

The propagation of structured light through obstacles is shown in Fig. 8(a). In here, the distance before encountering the obstacle as z_1, the self-healing process after encountering the obstacle as z_2, and the diameter of the obstacle as R. Throughout this propagation process, we can obtain the self-healing intensity affected by obstacles on the receiving plane as subgraph a1, the original intensity unaffected by obstacles on the receiving plane as subgraph a2, and the original intensity unaffected by obstacles at the location of the obstacle as subgraph a3. Figure 8(b) presents a flowchart detailing the inversion process for determining obstacle positions and sizes using the self-healing property. The intensity ratio can be obtained through the use of a1 and a2. Benefit from our previous research wherein it was determined that the intensity ratio remains unchanged during the whole self-healing process. Therefore, we can leverage the intensity ratio along with a3 to directly invert the diameter R of the obstacle. Upon obtaining the diameter of the obstacle, we can employ the obstacle information to produce the evolution curve of SSIM for PVB during its propagation through the obstacle. On the other hand, the SSIM of PVB on the receiving plane can be calculated using a1 and a2. By combining this with the obtained SSIM evolution curve, we can successfully invert the distance of the obstacle z_2. In Fig. 8(c), we present the results of two obstacle inversions using the self-healing property of PVB. The data validate the efficacy of our proposed method, demonstrating our ability to successfully determine the diameter of the obstacle as well as the distance. It is important to note that the SSIM evolution curve of the PVB may exhibit similar or even identical SSIM values at different propagation distance, which could potentially lead to errors in position inversion. To mitigate the impact of this limitation on the inversion model, the computational precision can be enhanced—such as increasing the SSIM calculation accuracy to six decimal places—thereby improving the discriminative capability and significantly reduce the likelihood of misidentification in exceptional cases. The obstacle inversion model we developed enables the practical application of the self-healing properties of structured light in optical systems. Furthermore, our study provides useful guidance for the development and utilization of self-healing property in optical applications. Theoretically, the model we have developed can be generalized to other forms of structured light with self-healing property.

In complex real-world transmission environments, structured light is inevitably subject to intense disruptions from turbulence channels[32]. This dynamic interaction process leads to significant stochastic attenuation of the structured light's intensity information. Hence, this phenomenon results in the intensity ratio of structured light during the self-healing process no longer remaining consistent, thus posing a significant challenge in accurately inverting the sizes and positions of obstacles. Convolutional neural networks (CNN) are deep feedforward neural architectures that employ convolutional operations to hierarchically extract features. They possess a strong capability to extract essential features from noise-contaminated samples. This enables CNN to learn intrinsic features during training, thereby establishing a precise mapping data from its disrupted state to its
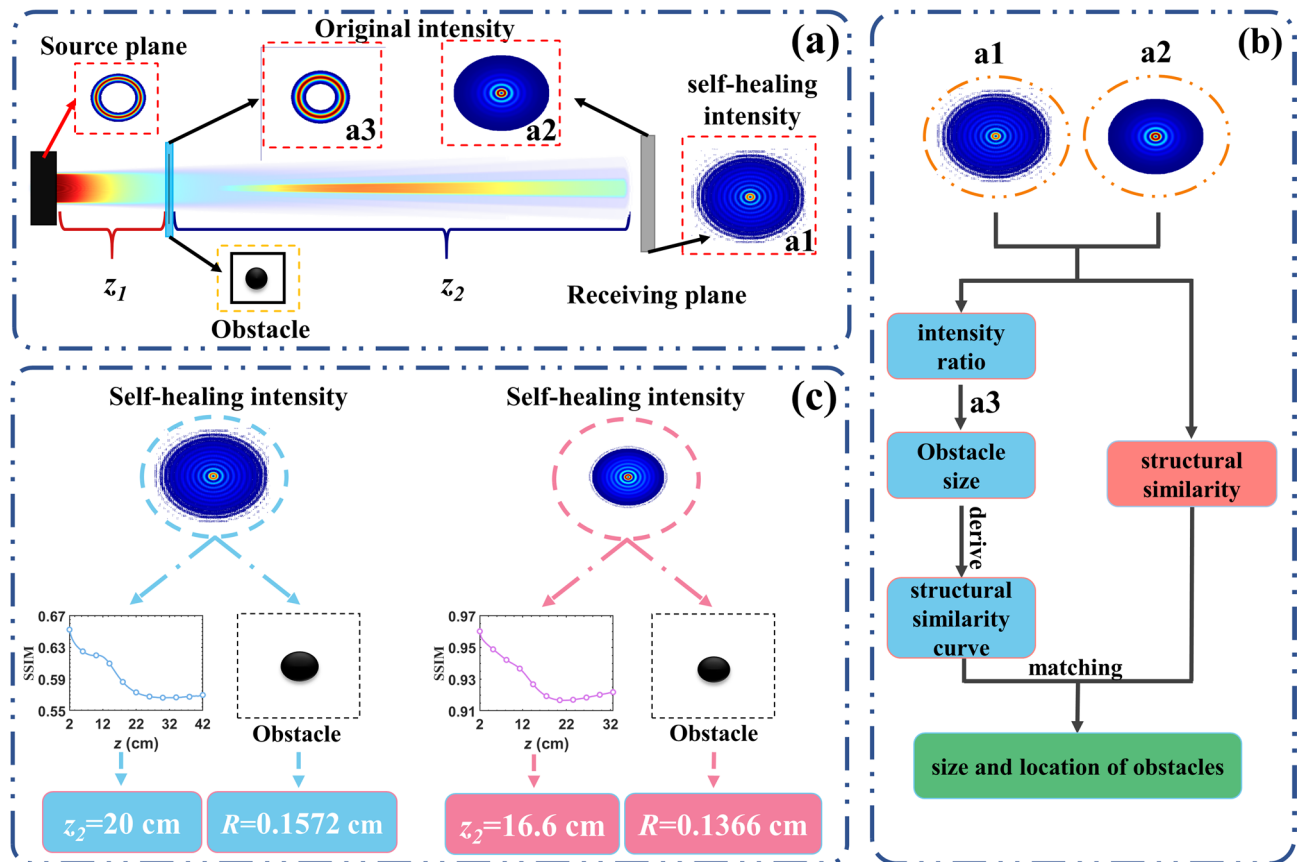
Fig. 8. (**a**) Schematic diagram of the propagation of structured light through an obstacle. Here, a2 and a3 respectively denote the original intensity of the unobstructed incident structured light at the obstacle and receiver planes, while a1 represents the self-healing intensity after encountering the obstacle. (**b**) Flowchart demonstrating obstacle inversion based on the self-healing property of structured light. (**c**) Results of the obstacle inversion model's testing.

original state. In view of this, we propose an innovative approach that utilizes CNN as a tool for suppressing turbulence effects. The objective is to eliminate disruptions introduced by turbulence channels, thereby restoring the structured light's original intensity information. Ultimately, this approach can aid in the inversion of obstacle size and position by obstacle inversion model.

As demonstrated in Fig. 9, the first step in our approach involves feeding a series of disrupted states affected by turbulence channels into the CNN for deep processing. The multi-level convolutional kernel architecture of CNN enables autonomous learning and efficient extraction of the essential features from disrupted states. These features exhibit a high degree of robustness to turbulence. Subsequently, we feed the corresponding original state into the CNN and establish an accurate mapping relationship with the essential features extracted by the CNN. This produces an optimized CNN model that supports the precise operation of subsequent obstacle inversion models. The self-healing intensity captured on the receiving plane in turbulence is inputted into the CNN. The CNN utilizes its powerful feature extraction ability to extract the essential features from the blurry intensity. It effectively eliminates turbulence-induced interference and output undisturbed intensity information data. Based on the data obtained from the output of CNN, we can effectively restore the self-healing intensity that has not been influenced by turbulence. Subsequently, the self-healing intensity can be incorporated into the obstacle inversion model to invert the size and position of obstacles. Figure 8 illustrates two sets of obstacle inversion results achieved through the use of our proposed obstacle inversion model. As shown in Fig. 9, even under the challenging conditions where turbulence significantly distorts the self-healing intensity information, the obstacle inversion model is not only able to invert the parameters of circular obstacles, but also effectively inversion of the parameters of rectangular obstacles. This robustly validates the effectiveness and reliability of our study. It should be noted that the current simulations were conducted under idealized conditions, assuming the system operates in a noise-free and interference-free environment. However, in actual experimental scenarios, the receiver may be affected by various environmental noise factors, which may adversely impact the stability and accuracy of the inversion model. Moving forward, we aim to validate the inversion process under real experimental conditions and optimize the model based on these results to further enhance its robustness and generalization ability in practical channels. Our research has made it possible to accurately invert the size and position of obstacles under turbulent conditions. This opens up a new technical pathway for further exploration in the field of optical
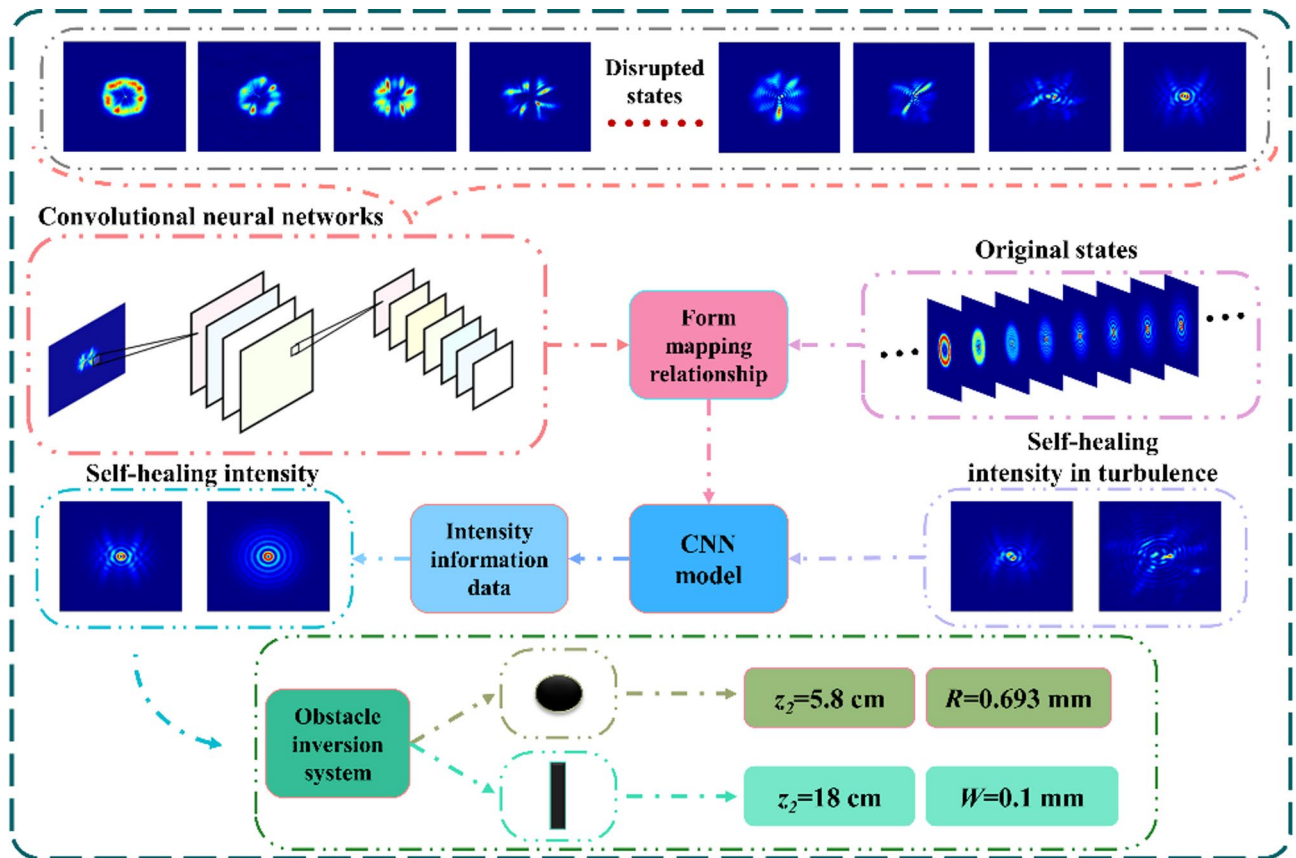
Fig. 9. The schematic diagram of the framework for obstacle inversion in oceanic turbulence using CNN. At the bottom are the test results of obstacle inversion system.

transmission, imaging technology, remote sensing science, and other related fields. Our study exhibits vast potential for application and significant scientific value.

Discussion

In this work, our preliminary research explored the impact of diverse obstacle shapes on PVB's self-healing property. Based on our findings, we established five conclusions regarding the self-healing property of structured light, which are as follows: (1) The self-healing of structured light requires the maximum retention of circular intensity information. (2) The self-healing of structured light exhibits a limit. (3) The self-focusing property of structured light have the potential to weaken the self-healing property. (4) The energy in the unobstructed region converges towards the two ends of the obstacle. (5) The self-healing process is divided into two parts - the obstructed region restoration, the unobstructed region damage. Theoretically, our conclusions are not limited to PVB and are applicable to other structured light as well.

Subsequently, we proposed a quantitative evaluation metric, namely SSIM of structured light, to assess the degree of self-healing exhibited by structured light based on its luminance, contrast, and structure evolution during the self-healing process. Our proposed SSIM is not only better aligned with the actual degree of self-healing exhibited by structured light, but can also be tailored to adjust the corresponding weightings based on the intended degree of demand for the self-healing property of structured light in terms of luminance, contrast, and structure in practical applications. Furthermore, we have investigated the essence of self-healing of structured light from the perspective of wave-particle duality. Our research has highlighted that structured light's self-healing is not a direct regeneration of the obstructed region, but rather a redistribution of the energy present in the unobstructed region. This interpretation has opened up a new perspective towards understanding the self-healing mechanisms present in structured light.

Building on the research outcomes outlined above, we have proposed a novel optical application model that utilizes the self-healing property of structured light for the inversion of obstacles. The utilization of the optical application model advanced in this research enables precision measurement of sizes and position of obstacles. This highlights the enormous potential of structured light's self-healing property in practical optical applications. Finally, given the inevitable influence of turbulent on the transmission of structured light in practical transmission environments. To overcome this challenge, we have implemented a novel approach by incorporating CNN into the proposed model to address the turbulence-induced disruption. This strategy allows for reliable inversion of obstacle sizes and position even under adverse conditions, characterized by severe blurring of structured light's intensity information due to the presence of turbulence. This research expands

not only the boundaries of applications for structured light's self-healing property in optics, but also provides a superior and more practical evaluation metric that enables more accurate quantitative assessments for the self-healing property for structured light. Our study lays a robust theoretical foundation and practical guidelines for the further exploration of the self-healing property of structured light.

Methods

The complex amplitude of the PVB at the source plane can be formulated as:

$$E_P\left(r, \varphi\right) = A_0 \exp\left(-\frac{r^2}{w_p^2}\right) I_{m_0}\left(\frac{2rr_0}{w_p^2}\right) \exp\left(im_0\varphi\right), \tag{6}$$

where (r, φ) represents the two dimensional position vector at the original plane, w_p represents the ring thickness of PVB, r_0 is defined as the ring radius. where f denotes the focal length of the Fourier lens, $k = 2\pi/\lambda$ is defined as the wave number of beams, λ is the wavelength of beam, $I_{m_0}(\cdot)$ is the modified Bessel function. To simulate the effect of obstacles, phase masks of various shapes were placed along the propagation axis of the beam. Each obstacle phase mask consists of a transparent region and an obstructing region. The transparent region allows the beam to propagate without perturbation, while the obstructing region absorbs the corresponding portion of the PVB, thereby effectively blocking its transmission through the obstructed area[3].

Turbulence-induced disruption are the predominant impact on the propagation of structured light in a transmission channel. The intensity of structured light is severely degraded during its propagation through the oceanic turbulence, as it is affected by refractive index fluctuations caused by variations in temperature and salinity of underwater medium. The phase screen method serves as a widely adopted and effective computational approach for modeling the influence of turbulence medium on the propagation dynamics of structured light[33,34]. This technique simulates turbulence-induced distortions by introducing random phase perturbations to the structured light's complex amplitude. Accordingly, the perturbed complex amplitude of the structured light after traversing the turbulent medium can be expressed as:

$$u_{out}\left(r, \varphi, z\right) = \mathcal{F}^{-1}\left\{\mathcal{F}\left\{E_P\left(r, \varphi\right) \exp\left[i\phi\left(r, \varphi\right)\right]\right\} \exp\left[\frac{-i\kappa^2\Delta z}{2k}\right]\right\}. \tag{7}$$

where $\mathcal{F}$ and $\mathcal{F}^{-1}$ respectively represents the Fourier transformation and inverse Fourier transformation, κ_x and κ_y are the spatial frequency component in the x and y directions, respectively, and $\phi(x, y)$ is defined as the spatial frequency domain representation of the phase:

$$\phi\left(x, y\right) = \sum_{\kappa_x}\sum_{\kappa_y} \frac{g\left(\kappa_x, \kappa_y\right)}{\sqrt{\Delta\kappa_x \Delta\kappa_y}} \sqrt{\Phi_n\left(\kappa\right)} \exp\left[i\left(\kappa_x x + \kappa_y y\right)\right], \tag{8}$$

where $g(\kappa_x, \kappa_y)$ is a two-dimensional complex random vector, $\Delta\kappa_x$ and $\Delta\kappa_y$ correspond to the grid sizes of the phase screen along the x and y directions, respectively. $\Phi_n(\kappa)$ denotes the spatial power spectrum, characterize turbulence-induced disruption affecting structured light in the oceanic environment. The spatial power spectrum model of oceanic turbulence can be expressed as follows[35,36]:

$$\Phi_n\left(\kappa\right) = \varepsilon^{-1/3}\beta A^2 \chi_T \frac{[1 + 4.6(\kappa\eta)^{2/3}]}{4\pi(\kappa^2 + \kappa_0^2)^{11/6}}$$
$$\left[\exp\left(-\frac{\kappa^2}{\kappa_T^2}\right) + \frac{1}{\varpi^2\theta_S}\exp\left(-\frac{\kappa^2}{\kappa_S^2}\right) - \frac{1 + \theta_S}{\varpi\theta_S}\exp\left(-\frac{\kappa^2}{\kappa_{TS}^2}\right)\right] \tag{9}$$

where ε denotes the turbulent kinetic energy dissipation rate of per unit mass of fluid, β is defined as the Obukhov-Corrsin constant, $A = 2.6 \times 10^{-4}$ liter/deg, $\kappa = \sqrt{\kappa_x^2 + \kappa_y^2}$ means the spatial frequency,

$\kappa_0 = 1/L_0$, L_0 is the outer scale of oceanic turbulence, ϖ is the contributions of temperature and salinity distributions to the refractive index fluctuations, $\kappa_i = R_i/\eta$, $R_i = [\sqrt{3}(W_i - 1/3 + 1/9W_i)]^{3/2}/Q^{3/2}$, $W_i = \{[\text{Pr}_i^2/(6\beta Q^{-2})^2 - \text{Pr}_i/81\beta Q^{-2}]^{1/2} - [1/27 - \text{Pr}_i/6\beta Q^{-2}]\}^{1/3}$, $(i = T, S, TS)$, Q means the non-dimensional constant, Pr_T and Pr_S denote the Prandtl numbers of temperature and salinity, respectively, $\text{Pr}_{TS} = 2\text{Pr}_T\text{Pr}_S/(\text{Pr}_T + \text{Pr}_S)$, χ_T indicates the rate of the dissipation of mean-squared temperature, θ_S means the ratio of the eddy thermal diffusivity coefficient to salt diffusivity coefficient.

The CNN utilized in our research is primarily composed of convolutional modules and linear layers. The convolutional module includes convolutional layers, normalization layers, and pooling layers. The convolutional layers extract local features of the self-healing intensity influenced by turbulence, generating a feature map through convolution kernel sliding. The pooling layers reduce the resolution of feature maps while preserving the essential features. Subsequently, the original self-healing intensity unaffected by turbulence is fed into the linear layers. Here, we establish a mapping relationship between the essential features extracted by the convolutional and pooling layers, and the original self-healing intensity. Ultimately, this enables the task of eliminating turbulence-induced effects on the self-healing intensity.

The structure of the CNN is shown in Fig. 10. The model uses the intensity distribution affected by turbulence disturbances as input training data, and the dimensions of the input intensity distribution are $X \in \mathbb{R}^{200 \times 200}$. For
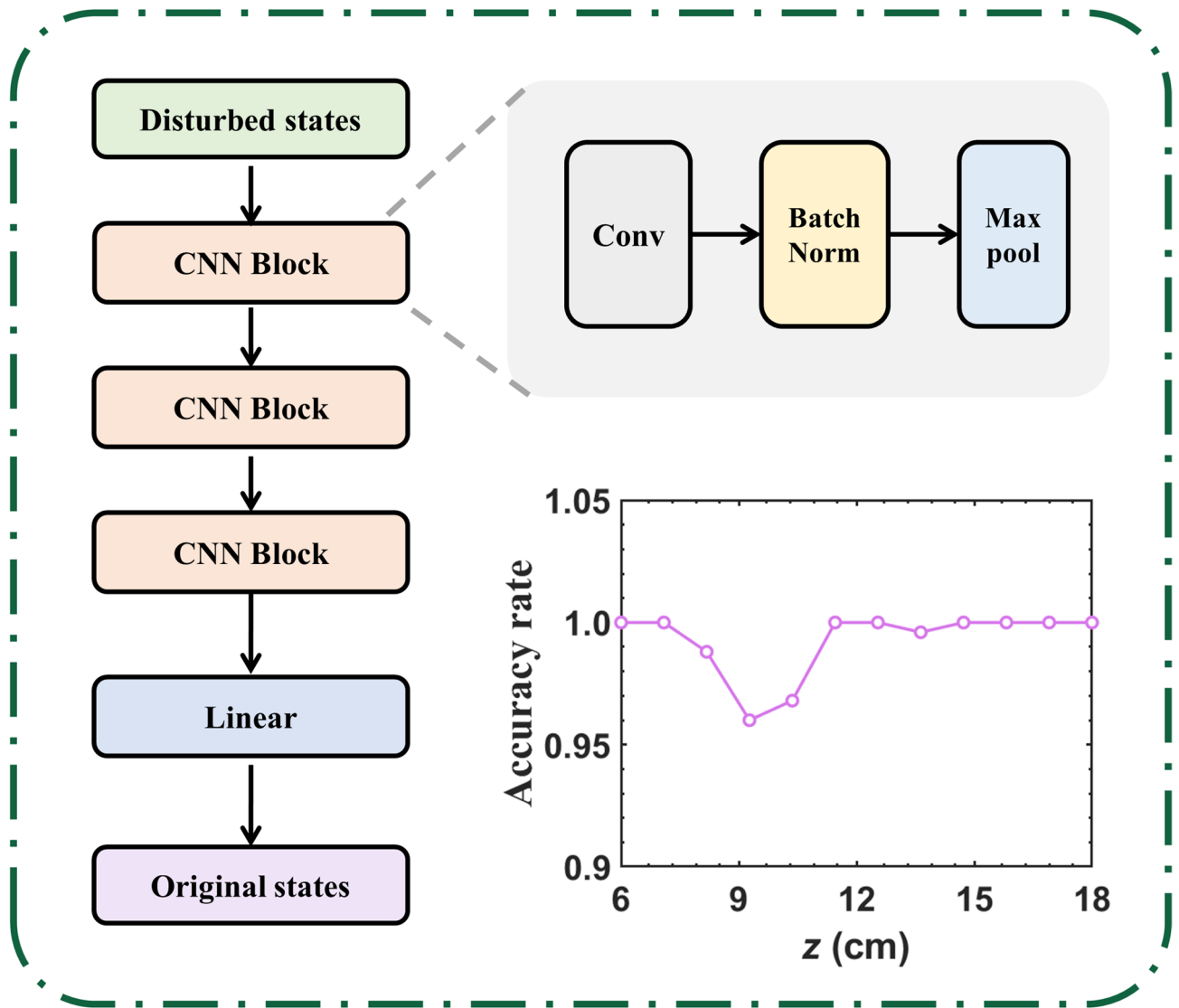
Fig. 10. The schematic diagram of the framework for the CNN architecture, along with the recognition accuracy of self-healing intensity distributions across varying propagation distances.

model training, the entire dataset is divided into training and validation sets in an 8:2 ratio to prevent overfitting and ensure the model's generalization ability. The output label *y* is a one-hot encoded vector corresponding to the original state, with the dimensionality of the label is determined by the predefined number of physical state categories. As illustrated in Fig. 10, the core of the model consists of a CNN feature extraction module and a linear classification layer. The CNN module comprises three convolutional layers: the first layer uses 64 3×3 convolutional kernels to extract local turbulence features, followed by further abstraction of the features using successive 3×3 convolutional kernels. After each convolutional layer, batch normalization is applied, and 2×2 max pooling is performed, which not only helps suppress overfitting but also gradually reduces the resolution of the feature map to 25×25. After the flatten operation, the feature vector is fed into a fully connected layer to establish the mapping $f : X \to p$, where the output is a probability distribution vector $p \in \mathbb{R}^k$, with *k* being the number of state categories. During the training process, the Adam optimizer is used to minimize the cross-entropy loss function:

$$L = -\sum\nolimits_{i=1}^{n} y_i \log\left(p_i\right) \qquad (6)$$

where y_i denotes the one-hot encoded vector of the original state. To recover the original self-healing intensity unaffected by turbulence, we select the output with the highest predicted probability and transform it using the $y_{onehot} = [y_{onehot1}, y_{onehot2}, \cdots, y_{onehoti}]$. Here, the y_{onehot} is subjected to the following condition:

$$y_{\text{onehot}} = \begin{cases} 1 & \text{if } i = \arg\max_j(y_j) \\ 0 & \text{otherwise} \end{cases} \tag{7}$$

where $\arg\max_j(y_i)$ represents the index of the maximum value in the output vector. In this work, we set the initial learning rate to 0.001, with a batch size of 32, and enabled learning rate decay when the validation loss stagnated. The training termination condition was set to when the validation loss did not show significant improvement over 10 consecutive epochs. During the model inference phase, we select the index $\arg\max_j(y_i)$ corresponding to the maximum probability value, and convert y_i to the original self-healing intensity distribution using the predefined physical mapping relation. This method enables implicit modeling of turbulence disturbance features through end-to-end learning. Figure 10 illustrates the model's recognition accuracy for self-healing intensity distributions affected by turbulence at different locations. The results demonstrate that the trained model can effectively identifies turbulence-distorted self-healing intensity distributions at various positions, validating its recognition capability and generalization performance in complex turbulent environments.

Data availability
All data is provided within the manuscript.

References
1. MacDonald, R. P., Boothroyd, S. A., Okamoto, T., Chrostowski, J. & Syrett, B. A. Interboard optical data distribution by bessel beam shadowing. *Opt. Commun.* **122**, 169 (1996).
2. Bouchal, Z., Wagner, J. & Chlup, M. Self-reconstruction of a distorted nondiffracting beam. *Opt. Commun.* **151**, 207 (1998).
3. Li, S. & Wang, J. Adaptive free-space optical communications through turbulence using self-healing bessel beams. *Sci. Rep.* **7**, 43233 (2017).
4. Broky, J., Siviloglou, G. A., Dogariu, A. & Christodoulides, D. N. Self-healing properties of optical airy beams. *Opt. Express.* **16**, 12880 (2008).
5. Zhou, G., Chu, X., Chen, R. & Zhou, Y. Self-healing properties of cosh-Airy beams. *Laser Physics* **29**, 025001 (2019).
6. Chen, L., Wen, J., Sun, D. & Wang, L. Self-healing property of focused circular airy beams. *Opt. Express.* **28**, 36516 (2020).
7. Wang, L. et al. Focusing and self-healing characteristics of airy array beams propagating in self-focusing media. *Appl Phys. B* **125**, 165 (2019).
8. Kumari, A., Dev, V. & Pal, V. Autofocusing and self-healing of partially blocked circular airy derivative beams. *Opt Laser Technol* **168**, 109837 (2024).
9. Vaveliuk, P., Martínez-Matos, Ó., Ren, Y. X. & Lu, R. D. Dual behavior of caustic optical beams facing Obstacles. *Phys Rev. A* **95**, 063838 (2017).
10. Zannotti, A., Denz, C., Alonso, M. A. & Dennis, M. R. Shaping caustics into propagation-invariant light. *Nat. Commun.* **11**, 3597 (2020).
11. Aiello, A. & Agarwal, G. S. Wave-optics description of self-healing mechanism in bessel beams. *Opt. Lett.* **39**, 6819 (2014).
12. Aiello, A. et al. Sanchez-Soto, L. L. Unraveling beam self-healing. *Opt. Express.* **25**, 19147 (2017).
13. Wang, F., Chen, Y., Liu, X., Cai, Y. & Ponomarenko, S. A. Self-reconstruction of partially coherent light beams scattered by opaque Obstacles. *Opt. Express.* **24**, 23735 (2016).
14. Martinez-Herrero, R., Juvells, I. & Carnicer, A. On the physical realizability of highly focused electromagnetic field distributions. *Opt. Lett.* **38**, 2065 (2013).
15. Chu, X. & Wen, W. Quantitative description of the self-healing ability of a beam. *Opt. Express.* **22**, 6899 (2014).
16. Garces-Chavez, V., McGloin, D., Melville, H., Sibbett, W. & Dholakia, K. Simultaneous micromanipulation in multiple planes using a self-reconstructing light beam. *Nature* **419**, 145 (2002).
17. McLaren, M., Mhlanga, T., Padgett, M. J., Roux, F. S. & Forbes, A. Self-healing of quantum entanglement after an obstruction. *Nat. Commun.* **5**, 3248 (2014).
18. He, C., Shen, Y. & Forbes, A. Towards higher-dimensional structured light. *Light Sci. Appl.* **11**, 205 (2022).
19. Forbes, A. & Nape, I. Quantum mechanics with patterns of light: progress in high dimensional and multidimensional entanglement with structured light. *AVS Quantum Science* **1**, 011701 (2019).
20. Nape, I., Sephton, B., Ornelas, P., Moodley, C. & Forbes, A. Quantum structured light in high dimensions. *APL Photonics* **8**, 051101 (2023).
21. Shen, Y., Pidishety, S., Nape, I. & Dudley, A. Self-healing of structured light: a review. *J. Opt.* **24**, 103001 (2022).
22. Ostrovsky, A. S., Rickenstorff-Parrao, C. & Arrizon, V. Generation of the perfect optical vortex using a liquid-crystal Spatial light modulator. *Opt. Lett.* **38**, 534 (2013).
23. Vaity, P. & Rusch, L. Perfect vortex beam: fourier transformation of a bessel beam. *Opt. Lett.* **40**, 597 (2015).
24. Shen, Y. et al. Optical vortices 30 years on: OAM manipulation from topological charge to multiple singularities. *Light Sci. Appl.* **8**, 1 (2019).
25. Willner, A. E. et al. Optical communications using orbital angular momentum beams. *Adv. Opt. Photon.* **7**, 66 (2015).
26. Yan, Q., Yu, L. & Zhang, Y. Effects of system pointing error and turbulence media anisotropy on the propagation of a perfect Laguerre-Gaussian vortex beam. *Waves Random Complex. Media*, 1 (2023).
27. Wang, W. et al. Evolution properties and Spatial-Mode UWOC performances of the perfect Vortex beam subject to oceanic turbulence. *IEEE Trans. Commun.* **69**, 7647 (2021).
28. Yu, J., Miao, C., Wu, J. & Zhou, C. Circular Dammann gratings for enhanced control of the ring profile of perfect optical vortices. *Photon Res* **8**, 648 (2020).
29. Tkachenko, G., Chen, M., Dholakia, K. & Mazilu, M. Is it possible to create a perfect fractional vortex beam? *Optica* **4**, (2017).
30. Chen, M., Mazilu, M., Arita, Y., Wright, E. M. & Dholakia, K. Dynamics of microparticles trapped in a perfect vortex beam. *Opt. Lett.* **38**, 4919 (2013).
31. Wang, Z., Bovik, A. C., Sheikh, H. R. & Simoncelli, E. P. Image quality assessment: from error visibility to structural similarity. *IEEE Trans. Image Process.* **13**, 600 (2004).
32. Ren, Y. et al. Orbital angular Momentum-based space division multiplexing for High-capacity underwater optical communications. *Sci. Rep.* **6**, 33306 (2016).
33. McGlamery, B. L. Restoration of Turbulence-Degraded images. *J. Opt. Soc. Am. A.* **57**, 293 (1967).

34. Zhou, H. et al. Atmospheric turbulence strength distribution along a propagation path probed by longitudinally structured optical beams. *Nat. Commun.* **14**, 4701 (2023).
35. Nikishov, V. V. & Nikishov, V. I. Spectrum of turbulent fluctuations of the sea-water refraction index. *Int. J. Fluid Mech. Res.* **27**, 82 (2000).
36. Yang, D., Zhang, Y. & Shi, H. Capacity of turbulent ocean links with carrier Bessel-Gaussian localized vortex waves. *Appl. Opt.* **58**, 9484 (2019).

Acknowledgements

Author contributions

S. W developed the concept and wrote the manuscript. Z. Z was responsible for the convolutional neural network part of the research. J. X, Y. Y and M. C reviewed and revised the manuscript.

Declarations

Competing interests

The authors declare no competing interests.

Additional information

Correspondence and requests for materials should be addressed to J.X. or Y.Y.

Reprints and permissions information is available at www.nature.com/reprints.

Publisher's note Springer Nature remains neutral with regard to jurisdictional claims in published maps and institutional affiliations.